Frontiers of Information Technology & Electronic Engineering
www.zju.edu.cn/jzus; engineering.cae.cn; www.springerlink.com
ISSN 2095-9184 (print); ISSN 2095-9230 (online)
E-mail: jzus@zju.edu.cn

A high precision visual localization sensor and its working methodology for an indoor mobile robot*

Feng-yu ZHOU†1, Xian-feng YUAN†‡1, Yang YANG2, Zhi-fei JIANG1, Chen-lei ZHOU1
(1School of Control Science and Engineering, Shandong University, Jinan 250061, China)
(2School of Information Science and Engineering, Shandong University, Jinan 250100, China)
†E-mail: zhoufengyu@sdu.edu.cn; yuanxianfeng_sdu@126.com

Received Aug. 21, 2015; Revision accepted Jan. 13, 2016; Crosschecked Mar. 9, 2016

Abstract: To overcome the shortcomings of existing robot localization sensors, such as low accuracy and poor robustness, a high precision visual localization system based on infrared-reflective artificial markers is designed and illustrated in detail in this paper. First, the hardware system of the localization sensor is developed. Secondly, we design a novel kind of infrared-reflective artificial marker whose characteristics can be extracted by the acquisition and processing of the infrared image. In addition, a confidence calculation method for marker identification is proposed to obtain the probabilistic localization results. Finally, the autonomous localization of the robot is achieved by calculating the relative pose relation between the robot and the artificial marker based on the perspective-3-point (P3P) visual localization algorithm. Numerous experiments and practical applications show that the designed localization sensor system is immune to the interferences of the illumination and observation angle changes. The precision of the sensor is ±1.94 cm for position localization and ±1.64° for angle localization. Therefore, it satisfies perfectly the requirements of localization precision for an indoor mobile robot.

Key words: Mobile robot, Localization sensor, Visual localization, Infrared-reflective marker, Embedded system
http://dx.doi.org/10.1631/FITEE.1500272 **CLC number:** TP242.6

1 Introduction

With the rapid development of robot techniques and an apparent urgent demand from the society, the indoor mobile robot will have a wide range of applications and provide services in diverse areas, such as transport, entertainment, and as a companion (Kim and Yoon, 2014; Luo and Lai, 2014; Yuan *et al.*, 2015). Rapid and accurate autonomous localization is essential for the completion of these intelligent services. General autonomous localization methods include mainly dead reckoning based on an odometer (Reinstein and Hoffmann, 2013), algorithms based on wireless sensor networks (Luo and Chen, 2013), inertial sensor based algorithms (Müller and Burgard, 2013), map-matching algorithms based on vision (Yu *et al.*, 2013), etc. However, these kinds of methods by themselves have low accuracy and poor robustness.

With advantages of high accuracy and non-cumulative error, localization methods based on artificial markers have been proposed and applied in indoor robot localization gradually over recent years (Lu W *et al.*, 2015; Lu Y and Song, 2015). Wu *et al.* (2013) designed a new kind of artificial marker based on the improved quick response (QR) code

---

‡ Corresponding author

[*] Project supported by the National High-Tech R&D Program (863) of China (No. 2009AA04Z220), the National Natural Science Foundation of China (No. 61375084), and the Key Program of Shandong Provincial Natural Science Foundation, China (No. ZR2015QZ08)

ORCID: Xian-feng YUAN, http://orcid.org/0000-0002-6217-6429

markers. This method is used to calculate the position coordinates of the robot based on landmark corner information extracted by the Harris corner measurement algorithm, but it is greatly affected by observation angles and cannot guarantee real-time operation because of its need to constantly adjust the robot pose. Kroumov and Okuyama (2012) achieved map building and navigation localization of a mobile robot through the vision-based simultaneous localization and mapping (SLAM) technique based on the artificial markers. However, it also cannot meet the requirements of real-time localization of a mobile robot because of its high complexity. Based on artificial markers, Aleksandrovich *et al.* (2013) designed a visual localization system which is able to achieve rapid localization with the pan-tilt camera and a laptop. However, the localization precision may easily be affected by illumination variation. To reduce the interference of illumination variation, visual localization techniques based on infrared markers are getting more attention (Her *et al.*, 2012; Oh *et al.*, 2014). Using light-emitting diodes (LEDs) as artificial landmarks, Ren *et al.* (2014) realized the localization of the robot based on a visual localization algorithm, but this method cannot meet the demands of navigation and positioning in a large-scale space as the landmarks cannot be numbered. Sultan *et al.* (2013) designed a kind of artificial marker based on an infrared dot-matrix and presented its corresponding algorithm which could identify markers by identity (ID). However, this method is inappropriate for use in the home environment due to its complex structure and high cost.

To solve existing problems, we design an embedded visual localization sensor system composed of an infrared image acquisition and processing unit installed on the robot and some infrared-reflective artificial markers pasted on the ceiling. During the motion of the robot, the sensor acquires real-time infrared images of artificial markers and computes the relative pose relation between the robot and markers using the perspective-3-point (P3P) visual localization algorithm after the preprocessing of image data. With the advantages of fast speed, high precision, strong robustness, and non-cumulative error, the sensor is able to evaluate the results of visual localization in real time and output the confidence level, which realizes the probabilistic localization. In addition, it is convenient to connect this localization sensor to the robot because of its small size. The results of experiments and practical applications show that it satisfies the requirements of rapid autonomous navigation of the indoor mobile robot perfectly.

2 Hardware system of the localization sensor

The overall framework of the localization sensor hardware system is illustrated in Fig. 1. It mainly consists of the following components:

1. A 32-bit high-performance fixed-point digital

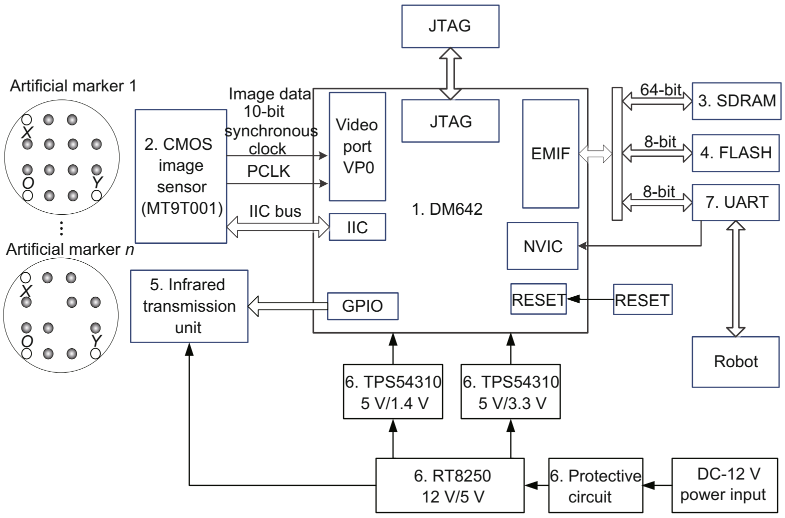

Fig. 1 Hardware framework of the localization sensor

signal processor (DSP), DM642 (Texas Instruments, USA), which is used for image processing and marker localization;

2. A 10-bit complementary metal-oxide semiconductor (CMOS) image sensor with high frame rate of exposure, MT9T001 (Micron, USA), which is responsible for the collection of infrared marker images;

3. A 32-MB SDRAM;

4. A 1 MB×8 bits flash chip, which stores the program code, marker data, and sensor configuration information;

5. An infrared transmission unit, which is composed of a circular array of 12 infrared diodes evenly distributed around the CMOS camera emitting infrared light to the artificial markers on the ceiling to make the images bright and clear;

6. A high reliability power supply unit, which will convert the DC-12 V input to DC-5 V, DC-3.3 V, and DC-1.4 V outputs for the power supply of the whole system (composed of a DCDC chip RT8250, two pieces of low dropout and high precision linear regulators TPS54310, and protective devices);

7. A serial-port communication unit.

3 Design of the infrared-reflective artificial marker

As shown in Fig. 1, the infrared-reflective artificial marker is composed of at most 15 marker dots and at least 3 marker dots. The horizontal and vertical spacings are all 4 cm between every two adjacent marker dots whose radii are 1 cm. All marker dots, which are made of retroreflective material (Nakamura and Suzuki, 2014) with high reflectivity to infrared light, are pasted on a film substrate. Since the marker dots can reflect more than 90% of the infrared coming from the infrared emitting unit, we can obtain the bright and clear marker images from which the feature information can be extracted easily. To obtain the unique marker identification direction, marker dots are divided into direction dots and coded dots. Direction dots, i.e., the three corner dots X, O, Y in the artificial marker, are used to calculate the angle and position coordinates of the robot in the marker coordinate system. All the other marker dots are called coded dots whose coding weights vary with their positions. In making markers, three direction dots must be pasted with reflection material, while the remaining 12 coded dots are optional, so we can obtain artificial markers with different IDs using different combinations of the coded dots. The number of possible marker IDs is $2^{12} = 4096$, which completely satisfies the autonomous localization requirement of the robot in a wide range of indoor environments.

4 Extraction and recognition of the artificial marker image

4.1 Optimal localization marker extraction and confidence calculation

To realize accurate robot localization, we first need to extract the optimal localization marker from the image captured by the localization sensor. As an original image captured by the localization sensor, Fig. 2a indicates that the gray values of the marker dots pasted with infrared reflection material are close to 255, so accurate segmentation of the marker and background images can be achieved by a fixed threshold value. Fig. 2b, a binary image whose threshold value is set to 200, still contains the interference areas such as fluorescent tube. These areas can be taken out by limiting the connected area and aspect ratio. The robot will automatically choose the marker closest to the image center as the optimal localization marker when there are multiple markers in the view of the robot. The selection process of the optimal marker includes mainly four steps: (1) Erosion is done to the marker binary image to avoid adherence of different marker dots under the highlighted area. (2) Dilation is performed to connect different marker dots as a whole. (3) As shown in Fig. 2c, the Euclidean distances from the center point of each marker dilation area such as $B(x_b, y_b)$ and $C(x_c, y_c)$, are calculated by

$$\begin{cases} d_{\mathrm{AB}} = \sqrt{(x_a - x_b)^2 + (y_a - y_b)^2}, \\ d_{\mathrm{AC}} = \sqrt{(x_a - x_c)^2 + (y_a - y_c)^2}. \end{cases} \tag{1}$$

The area with minimum distance is the optimal localization marker dilation area under the robot's current position. (4) The local 'image and' operation is used between the optimal localization marker dilation area and the corroded marker image to calculate the optimal original localization marker area

(Fig. 2d). The method of choosing the optimal localization marker is similar when there are more than two markers in the view of the sensor.

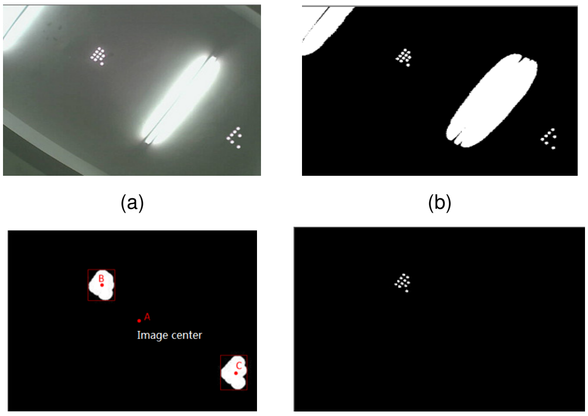

(a) (b)

(c) (d)

Fig. 2 Optimal marker extraction: (a) original image; (b) binary image; (c) image dilation; (d) optimal marker

To acquire the probabilistic localization result for the fusion of the multiple sensors, a confidence modeling calculation is necessary for markers extracted by the localization sensor. To this end, in this study we propose a probabilistic marker confidence modeling calculation method. First, gray histogram statistics of the marker dots are obtained based on 200 binary marker images as shown in Fig. 2d and the statistical results are shown in Fig. 3. Second, we adopt the Gaussian curve-fitting approach to process the gray values of marker dots as shown in Fig. 3 and the results are shown in Fig. 4. We can obtain the fitting function

$$\begin{aligned} f(x) =& 2634 \times \mathrm{e}^{-(x-245.4)^2/196.84} \\ &+ 525 \times \mathrm{e}^{-(x-208.6)^2/791.30}, \end{aligned} \tag{2}$$

where x is the gray value.

It can be seen from Eq. (2) and Fig. 4 that the maximum and minimum gray values of the marker dots are $H_{\max} = 2730.3$ and $H_{\min} = 478.2$, respectively.

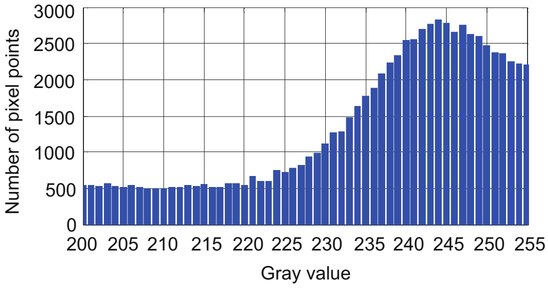

Fig. 3 Statistical results of the infrared-reflective markers in gray values

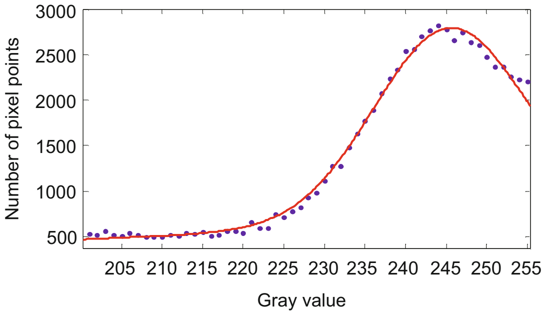

Fig. 4 Distribution curve of the infrared-reflective markers in gray values

Denote by N the total number of all reflective pixel points among marker S, x_i the gray value of the ith reflective pixel point of marker S, and n_{x_i} the number of pixel points with the corresponding gray value. Then the confidence of marker S, which is crucial to multi-sensor information fusion, can be defined as follows:

$$P(S) = \frac{1}{N}\left(\sum_{x_i=200}^{255} \frac{f(x_i) - H_{\min}}{H_{\max} - H_{\min}} \times n_{x_i}\right), \tag{3}$$

where $P(S)$ is the confidence of marker S and $f(\cdot)$ the fitting function shown in Eq. (2).

4.2 Calculation of the characteristic parameters of the marker

4.2.1 Establishment of the marker image coordinate system

For the establishment of the XOY coordinate system in marker images, we need to identify the three direction dots of the artificial marker, i.e., X, O, and Y. First of all, the linear distances between any two marker dots are calculated and the two endpoints of the longest distance are marked as A and B. Then the distances of all marker dots to the midpoint of line AB are calculated and the marker dot corresponding to the longest distance is O. As illustrated in Fig. 5a, points O, A, B are defined as the direction points. Next, we need to identify the X and Y axes for the unique establishment of the marker image coordinate system. Given that the pixel coordinates of point O are (x_1, y_1) and either point A or B is selected to rotate around point O 90° clockwise (Fig. 5b), the pixel coordinates of the selected point are marked as (x_2, y_2), and the pixel coordinates of the unselected point are denoted by (x_3, y_3). So, we can obtain the calculation formula of pixel coordinates (x, y) of point P as follows:

$$\begin{cases} x = (x_2 - x_1)\cos\alpha - (y_2 - y_1)\sin\alpha + x_1, \\ y = (y_2 - y_1)\cos\alpha - (x_2 - x_1)\sin\alpha + y_1, \end{cases} \tag{4}$$

where α indicates the rotation angle. Then we can calculate angle δ between vector $\vec{OU}$ (from O to the unselected point (in Fig. 5b, point U overlapped with point A)) and vector $\vec{OP}$:

$$\cos\delta = \frac{(x - x_1)(x_3 - x_1) + (y - y_1)(y_3 - y_1)}{\sqrt{(x - x_1)^2 + (y - y_1)^2}\sqrt{(x_3 - x_1)^2 + (y_3 - y_1)^2}}. \tag{5}$$

If $\cos\delta > 0$, the angle between the two vectors is an acute angle and (x_2, y_2) corresponds to the X axis and (x_3, y_3) corresponds to the Y axis. Otherwise, (x_2, y_2) corresponds to the Y axis and (x_3, y_3) corresponds to the X axis.

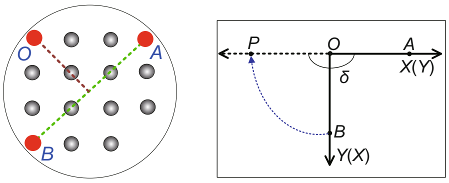

(a) (b)

Fig. 5 Marker image coordinate system: (a) identification of the direction dots; (b) identification of the axis

4.2.2 Identification of the marker's ID

As shown in Fig. 6, we can establish the marker image coordinate system XOY on the camera imaging plane $X'O'Y'$ after the identification of direction points and X, Y axes. Given that the image coordinates of points O and Y are (x_o, y_o), (x_y, y_y) respectively, we need to identify the coded dots based on the geometrical characteristics of the marker. Then we can calculate the ID of the marker according to the distribution of coded dots and the corresponding weighting values.

The steps of detecting the coded dots are as follows:

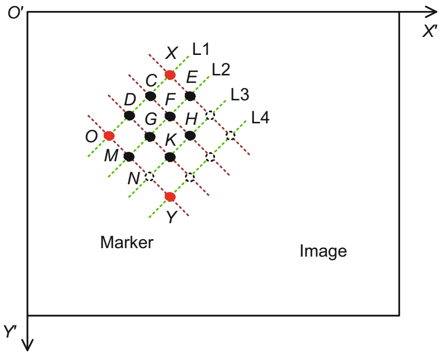

Fig. 6 Infrared-reflective marker image coordinate system

Step 1: No matter whether M and N are coded dots, the image coordinates of M and N can be computed by the relation with vector $\vec{OY}$ in the marker coordinate system XOY. Given that the image coordinates of M and N are (x_m, y_m) and (x_n, y_n) respectively, we can obtain

$$\begin{cases} (x_m - x_o, y_m - y_o) = \dfrac{1}{3}(x_y - x_o, y_y - y_o), \\ (x_n - x_o, y_n - y_o) = \dfrac{2}{3}(x_y - x_o, y_y - y_o). \end{cases} \tag{6}$$

Step 2: We take T as any one of the coded dots in the marker and $R \in \{O, M, N, Y\}$ as a loop variable, and the image coordinates of variables R and T are (x_r, y_r) and (x_t, y_t), respectively. Then the angle threshold (α) and amplitude threshold (λ) between vector $\vec{RT}$ and vector $\vec{OY}$ can be obtained as follows:

$$\begin{aligned} \alpha = \arccos\Big(& [(x_t - x_r)(x_y - x_o) + (y_t - y_r)(y_y - y_o)] \\ & \cdot [(x_t - x_r)^2 + (y_t - y_r)^2]^{-1/2} \\ & \cdot [(x_y - x_o)^2 + (y_y - y_o)^2]^{-1/2} \Big), \end{aligned} \tag{7}$$

$$\lambda = \frac{\sqrt{(x_t - x_r)^2 + (y_t - y_r)^2}}{\sqrt{(x_y - x_o)^2 + (y_y - y_o)^2}}. \tag{8}$$

Step 3: According to α and λ, we determine whether the corresponding coded dot exists or not. For example, when R equals M, we consider coded dot G exists if α is near 90° and λ is near $1/3$. If λ is near $2/3$, we consider that coded dot F exists and it is similar to other coded dots.

After all the coded dots are identified, we can calculate the marker ID according to the weight matrix of the marker dots:

$$\mathrm{ID} = \sum_{i=1}^{4}\sum_{j=1}^{4} W(i, j) \cdot Q(i, j) = 1782, \tag{9}$$

where

$$\boldsymbol{W}=\begin{bmatrix}0 & 1 & 0 & 0\\ 1 & 1 & 1 & 0\\ 1 & 1 & 1 & 0\\ 0 & 1 & 0 & 0\end{bmatrix}$$

and

$$\boldsymbol{Q}=\begin{bmatrix}0 & \text{0x020} & \text{0x200} & 0\\ \text{0x002} & \text{0x010} & \text{0x100} & \text{0x800}\\ \text{0x001} & \text{0x008} & \text{0x080} & \text{0x400}\\ 0 & \text{0x004} & \text{0x040} & 0\end{bmatrix}$$

are the weight matrix and the coded matrix of the sample marker (Fig. 6), respectively.

5 P3P based visual localization algorithm

In this study, robot pose estimation is achieved by a P3P visual localization algorithm (Vynnycky and Kanev, 2015). As shown in Fig. 7, a marker perspective projection model is established, where CP is the camera optical axis center, X, O, Y are the three direction dots of the marker, and X', O', Y' are the corresponding perspective projection points on the imaging plane.

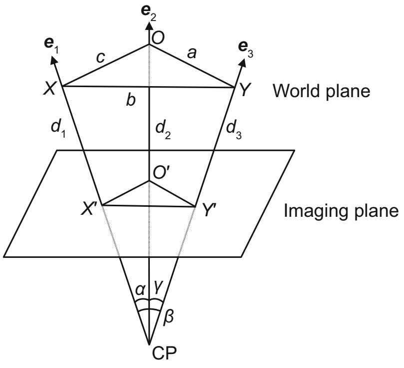

Fig. 7 Infrared-reflective marker perspective projection model

As shown in Fig. 7, given a, b, c as the sides of the spatial triangle composed of the three marker direction dots X, O, Y, the straight-line distance and unit direction vector from CP to X, O, Y are d_1, d_2, d_3 and $\boldsymbol{e}_1$, $\boldsymbol{e}_2$, $\boldsymbol{e}_3$ respectively, and the angles between every two of $\boldsymbol{e}_1$, $\boldsymbol{e}_2$, $\boldsymbol{e}_3$ are α, β, and γ. The equations can be built according to the triangular geometry relationship as follows (Xu *et al.*, 2011):

$$\begin{cases} d_1^2+d_2^2-2d_1d_2\cos\alpha=c^2,\\ d_1^2+d_3^2-2d_1d_3\cos\beta=b^2,\\ d_2^2+d_3^2-2d_2d_3\cos\gamma=a^2,\end{cases} \tag{10}$$

where

$$\begin{cases} \cos\alpha=\boldsymbol{e}_1^{\mathrm{T}}\boldsymbol{e}_2,\\ \cos\beta=\boldsymbol{e}_1^{\mathrm{T}}\boldsymbol{e}_3,\\ \cos\gamma=\boldsymbol{e}_2^{\mathrm{T}}\boldsymbol{e}_3.\end{cases} \tag{11}$$

The camera internal matrix is $\boldsymbol{K}$, the image coordinates of X, O, Y are $(u_i, v_i, 1)^{\mathrm{T}}$ $(i=1,2,3)$, and the focal length normalization projective coordinates of the marker direction dots can be calculated as

$$\begin{bmatrix}{}^{\mathrm{c}}x_i\\ {}^{\mathrm{c}}y_i\\ 1\end{bmatrix}=\begin{bmatrix}k_x & 0 & u_0\\ 0 & k_y & v_0\\ 0 & 0 & 1\end{bmatrix}^{-1}\cdot\begin{bmatrix}u_i\\ v_i\\ 1\end{bmatrix},\ i=1,2,3. \tag{12}$$

Given these, we can obtain the unit direction vector $\boldsymbol{e}_i$ $(i=1,2,3)$ as follows:

$$\boldsymbol{e}_i=\frac{1}{\sqrt{{}^{\mathrm{c}}x_i^2+{}^{\mathrm{c}}y_i^2+1}}\begin{bmatrix}{}^{\mathrm{c}}x_i\\ {}^{\mathrm{c}}y_i\\ 1\end{bmatrix}. \tag{13}$$

Then we can calculate the straight-line distances d_1, d_2, d_3 from CP to direction dots X, O, Y according to Eqs. (10)–(13). The coordinates of direction dots X, O, Y in the camera coordinate system ${}^{\mathrm{c}}\boldsymbol{P}_i$ $(i=1,2,3)$ can be obtained as follows:

$${}^{\mathrm{c}}\boldsymbol{P}_i=d_i\boldsymbol{e}_i. \tag{14}$$

The coordinates of direction dots X, O, Y in the world coordinate system, which are already known when pasting the markers, can be marked as ${}^{\mathrm{w}}\boldsymbol{P}_i$ $(i=1,2,3)$. As the world and camera coordinate systems satisfy the transformational relation as shown in Eq. (15), the rotation matrix $\boldsymbol{R}_{\mathrm{w}}$ and translation matrix $\boldsymbol{t}_{\mathrm{w}}$ can be acquired based on the world coordinates ${}^{\mathrm{w}}\boldsymbol{P}_i$ $(i=1,2,3)$ and the camera coordinates ${}^{\mathrm{c}}\boldsymbol{P}_i$ $(i=1,2,3)$ of the marker direction dots X, O, Y:

$$\begin{cases} {}^{\mathrm{c}}\boldsymbol{P}_1=\boldsymbol{R}_{\mathrm{w}}{}^{\mathrm{w}}\boldsymbol{P}_1+\boldsymbol{t}_{\mathrm{w}},\\ {}^{\mathrm{c}}\boldsymbol{P}_2=\boldsymbol{R}_{\mathrm{w}}{}^{\mathrm{w}}\boldsymbol{P}_2+\boldsymbol{t}_{\mathrm{w}},\\ {}^{\mathrm{c}}\boldsymbol{P}_3=\boldsymbol{R}_{\mathrm{w}}{}^{\mathrm{w}}\boldsymbol{P}_3+\boldsymbol{t}_{\mathrm{w}}.\end{cases} \tag{15}$$

6 Experimental evaluation

Before experimenting, we need to calibrate the internal matrix of the camera. We use the camera calibration algorithm proposed by Zhang (2000), i.e., using 20 chessboard images taken from different angles as a calibration template. The internal matrix of the camera after calibration is as follows:

$$\boldsymbol{K}=\begin{bmatrix}755.139 & 0 & 320.252\\ 0 & 753.926 & 239.661\\ 0 & 0 & 1\end{bmatrix}. \tag{16}$$

6.1 Artificial marker identification experiment

To test the identification speed and precision of the localization sensor to artificial markers, we made 100 markers distinguished by IDs and carried out 200 marker identification experiments under different camera angles, illuminations, and quantities of markers. As shown in Table 1, experimental results showed that the marker identification accuracy of the localization sensor was up to 96% and that the processing speed of the markers was nearly 12 frames/s, which satisfy the requirements of real-time navigation and positioning for the robot.

6.2 Pose calculation experiment

First, we pasted an artificial marker on the ceiling, setting the direction dots O, X, Y as the origin, X axis, Y axis of the world coordinate system, respectively. By comparing the real pose coordinates of the measurement point with the output pose coordinates of the sensor, we tested the precision of the sensor. In addition, the confidence of marker recognition $P(S)$ was computed in real time using Eq. (2).

The pose detection experiment was divided into two parts. One was the angle test; i.e., the localization sensor was spun around every 30° at a time (Table 2). The other was the position test; i.e., the localization sensor moved along the direction of the Y axis and the position coordinates were measured every 10 cm (Table 3).

Experimental results showed that the average angle measurement deviation was $\pm 1.64°$ and the average position measurement deviation was ± 1.94 cm. Therefore, the localization sensor has a high precision localization ability and can meet the requirements of accurate navigation and positioning for a service robot in the home environment.

6.3 Navigation and positioning experiment

The indoor autonomous localization experiment was carried out based on the nursing mobile robot (Fig. 8) developed by our research group. For fast and accurate navigation and positioning, we pasted the artificial markers on the ceiling of our lab according to certain rules, and the absolute positions of the markers were known in advance. Fig. 9 shows the projection model of the localization sensor whose projective field is a circular area on the ceiling. The radius of the projective field is R and can be detected by the robot as long as there is a marker in it. As shown in Fig. 9, the distance h from the localization sensor to the ceiling is 1.5 m and the view angle of the camera α is 90°. So, R is 1.5 m; i.e., the maximum distance between markers is 3 m on condition that there is no assistance from other localization sensors.

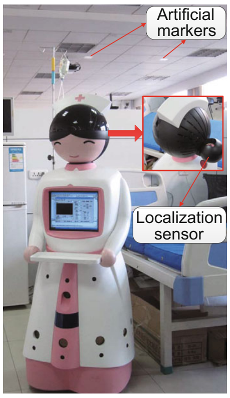

Fig. 8 Experimental robot

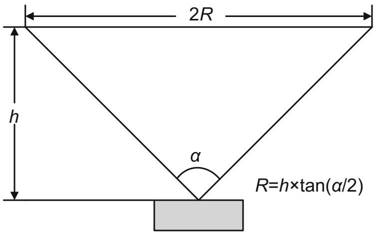

Fig. 9 Projection model of the localization sensor

As shown in Fig. 8, the localization sensor was mounted on the back of the robot's head instead of

Table 1 Experimental results of marker identification

Number of markers	Correct number	Accuracy	Mean elapsed time (ms)
200	192	96%	87

Table 2 Experimental results of angle test

Number	Real angle (°)	Output angle (°)	Measurement deviation (°)	Confidence
1	0	0.31	−0.31	0.94
2	30	29.12	0.88	0.92
3	60	62.38	−2.38	0.87
4	90	88.57	1.43	0.90
5	120	123.44	−3.44	0.84
6	150	146.82	3.18	0.85
7	180	181.03	−1.03	0.91
8	210	213.11	−3.11	0.85
9	240	239.65	0.35	0.94
10	270	269.35	0.65	0.93
11	300	301.98	−1.98	0.88
12	330	330.36	−0.36	0.94
13	360	2.23 (362.23)	−2.23	0.87

Table 3 Experimental results of position test

Number	Real position (cm)			Output position (cm)			Measurement deviation (cm)			Confidence,
	X_{R}	Y_{R}	Z_{R}	X_{M}	Y_{M}	Z_{M}	ΔX	ΔY	ΔZ	$P(S)$
1	−50.00	−50.00	260.00	−49.34	−49.19	261.17	−0.66	−0.81	−1.17	0.94
2	−50.00	−40.00	260.00	−51.63	−41.02	258.71	1.63	1.02	1.29	0.88
3	−50.00	−30.00	260.00	−51.29	−28.87	260.80	1.29	−1.13	−0.80	0.91
4	−50.00	−20.00	260.00	−48.15	−20.93	259.07	−1.85	0.93	0.93	0.88
5	−50.00	−10.00	260.00	−49.16	−11.79	261.17	−0.84	1.79	−1.17	0.88
6	−50.00	0.00	260.00	−51.56	1.80	259.12	1.56	−1.80	0.88	0.86
7	−50.00	10.00	260.00	−48.95	8.63	261.40	−1.05	1.37	−1.40	0.89
8	−50.00	20.00	260.00	−49.05	19.86	261.12	−0.95	0.14	−1.12	0.95
9	−50.00	30.00	260.00	−50.56	30.44	258.76	0.56	−0.44	1.24	0.95
10	−50.00	40.00	260.00	−51.27	38.77	260.06	1.27	1.23	−0.06	0.92
11	−50.00	50.00	260.00	−51.13	49.49	259.03	1.13	0.51	0.97	0.94

the body center. Hence, it is necessary to transform the sensor output position coordinates into the coordinates described in the robot coordinate system. The sensor position compensation model is shown in Fig. 10, where $(X_{\mathrm{W}}, Y_{\mathrm{W}})$ is the world coordinate system, $(X_{\mathrm{R}}, Y_{\mathrm{R}})$ represents the robot coordinate system whose origin is the robot's center, and $(X_{\mathrm{T}}, Y_{\mathrm{T}})$ denotes the localization sensor coordinate system whose origin is the sensor's center. To compensate for the installation deviation of the localization sensor, the robot was controlled to spin around five times and the outputs of the localization sensor were recorded. Then the rotation radius r of the robot could be calculated by a least squares circle fitting algorithm.

Given the position coordinates (x_t, y_t) and angle θ detected by the localization sensor at some point, the robot's real position coordinates after deviation compensation can be calculated as

$$\begin{cases} x_{\mathrm{r}} = x_t - r\cos\theta, \\ y_{\mathrm{r}} = y_t - r\sin\theta. \end{cases} \tag{17}$$

The position coordinates and heading angle provided by the localization sensor belong to open-loop information. Moreover, the nursing robot applies a dual wheel differential drive and unbalanced rotation of dual wheel is inevitable while in motion. Therefore, it is necessary to introduce a closed-loop control strategy to guarantee accurate path tracking. The robot navigation control model is shown in Fig. 11,

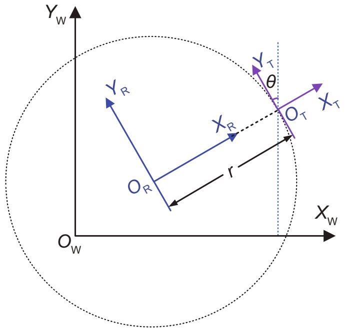

Fig. 10 Deviation compensation of sensor installation

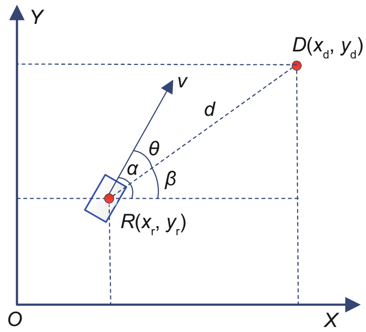

Fig. 11 Sketch map of the robot navigation control

where $R(x_\mathrm{r}, y_\mathrm{r})$ and $D(x_\mathrm{d}, y_\mathrm{d})$ indicate the current position and target position, respectively. Given that α and β are the angles between the current direction, target direction, and the X axis respectively, the robot steering angle θ can be calculated as follows:

$$\theta = \alpha - \beta = \alpha - \arctan\left(\frac{y_\mathrm{d} - y_\mathrm{r}}{x_\mathrm{d} - x_\mathrm{r}}\right). \tag{18}$$

The robot spun around θ degrees and then moved to the target point D along a straight line. The distance d between the current position R and target position D was calculated in real time while in motion:

$$d = \sqrt{(x_\mathrm{d} - x_\mathrm{r})^2 + (y_\mathrm{d} - y_\mathrm{r})^2} \leq \varepsilon, \tag{19}$$

where ε is a small positive number and represents the positioning precision. We can consider that the robot has arrived at the target point only if d satisfies the precision requirement.

Before the indoor navigation and positioning experiment, the occupancy grid map (resolution: 0.05 m) of our lab (size: 15.3 m×7.5 m) was obtained (Fig. 12). In the figure, the black grids represented the obstacles such as partition wall and tables, and the orange dots were artificial markers pasted on the ceiling. To test and verify the accuracy of the designed localization sensor, the experimental robot moved along the path preplanned using the A* algorithm (Persson and Sharf, 2014). The red curve was the planned ideal curve, and S and E were the start and end points of the planned path, respectively. Then the robot was controlled to track the planned path based on the closed-loop control strategy and the blue circles were the recorded practical motion track. From the compound degree of the two curves, we can draw the conclusion that the robot can achieve accurate autonomous navigation in real time based on the designed localization sensor.

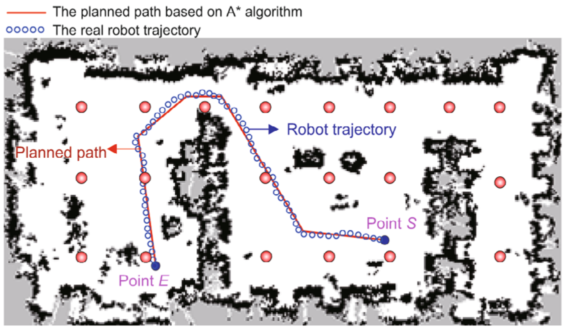

Fig. 12 Robot self-localization results in a home environment (references to color refer to the online version of this figure)

7 Conclusions

To address the problems existing in the autonomous indoor localization of a service robot, we design an embedded visual localization sensor and a novel kind of dot-matrix infrared-reflective artificial marker. This localization system can not only provide a sufficient number of markers but also reduce the interference of illumination variation and observation angle on localization accuracy, which improves the robustness of the localization system efficiently. To obtain the probabilistic outputs of the localization sensor, we propose a novel confidence calculation method for marker identification based on statistical analysis of gray values of the marker dots. Using the P3P visual localization algorithm, we can calculate the relative pose relation between the robot and marker, based on which the world coordinates of the robot can be obtained. Experimental results indicate that the precision of the designed sensor is ±1.94 cm for position localization and ±1.64° for angle localization. The proposed visual localization sensor system satisfies the requirements of accurate autonomous indoor robot navigation and provides a novel indoor localization method for a home service robot.

References

Aleksandrovich, Y.D., Gennadievich, P.G., Stepanovich, K.A., *et al.*, 2013. Mobile robot navigation based on artificial landmarks with machine vision system. *World Appl. Sci. J.*, **24**(11):1467-1472.

Her, K.W., Kim, D.H., Ha, J.E., 2012. Localization of mobile robot using laser range finder and IR landmark. Proc. 12th Int. Conf. on Control, Automation and Systems, p.459-461.

Kim, Y., Yoon, W.C., 2014. Generating task-oriented interactions of service robots. *IEEE Trans. Syst. Man Cybern.*, **44**(8):981-994. http://dx.doi.org/10.1109/TSMC.2014.2298214

Kroumov, V., Okuyama, K., 2012. Localisation and position correction for mobile robot using artificial visual landmarks. *Int. J. Adv. Mech. Syst.*, **4**(2):112-119. http://dx.doi.org/10.1504/IJAMECHS.2012.048395

Lu, W., Xiang, Z., Liu, J., 2015. Design of an enhanced visual odometry by building and matching compressive panoramic landmarks online. *Front. Inform. Technol. Electron. Eng.*, **16**(2):152-165. http://dx.doi.org/10.1631/FITEE.1400139

Lu, Y., Song, D., 2015. Visual navigation using heterogeneous landmarks and unsupervised geometric constraints. *IEEE Trans. Robot.*, **31**(3):736-749. http://dx.doi.org/10.1109/TRO.2015.2424032

Luo, R.C., Chen, O., 2013. Wireless and pyroelectric sensory fusion system for indoor human/robot localization and monitoring. *IEEE/ASME Trans. Mech.*, **18**(3):845-853. http://dx.doi.org/10.1109/TMECH.2012.2188300

Luo, R.C., Lai, C.C., 2014. Multisensor fusion-based concurrent environment mapping and moving object detection for intelligent service robotics. *IEEE Trans. Ind. Electron.*, **61**(8):4043-4051. http://dx.doi.org/10.1109/TIE.2013.2288199

Müller, J., Burgard, W., 2013. Efficient probabilistic localization for autonomous indoor airships using sonar, air flow, and IMU sensors. *Adv. Robot.*, **27**(9):711-724. http://dx.doi.org/10.1080/01691864.2013.779005

Nakamura, T., Suzuki, S., 2014. Simplified EKF-SLAM by combining laser range sensor with retro reflective markers for use in kindergarten. *Int. J. Robot. Mech.*, **1**(1):1-7.

Oh, J.H., Kim, D., Lee, B.H., 2014. An indoor localization system for mobile robots using an active infrared positioning sensor. *J. Ind. Intell. Inform.*, **2**(1):35-38. http://dx.doi.org/10.12720/jiii.2.1.35-38

Persson, S.M., Sharf, I., 2014. Sampling-based A* algorithm for robot path-planning. *Int. J. Robot. Res.*, **33**(13):1683-1708. http://dx.doi.org/10.1177/0278364914547786

Reinstein, M., Hoffmann, M., 2013. Dead reckoning in a dynamic quadruped robot based on multimodal proprioceptive sensory information. *IEEE Trans. Robot.*, **29**(2):563-571. http://dx.doi.org/10.1109/TRO.2012.2228309

Ren, Y., Ye, A., Lu, T., *et al.*, 2014. A method of self-localization of robot based on infrared landmark. Proc. 11th World Congress on Intelligent Control and Automation, p.5494-5499. http://dx.doi.org/10.1109/WCICA.2014.7053654

Sultan, M.S., Chen, X., Qadeer, N., *et al.*, 2013. Vision guided path planning system for vehicles using infrared landmark. Proc. IEEE Int. Conf. on Robotics and Biomimetics, p.179-184. http://dx.doi.org/10.1109/ROBIO.2013.6739455

Vynnycky, M., Kanev, K., 2015. Mathematical analysis of the multisolution phenomenon in the P3P problem. *J. Math. Imag. Vis.*, **51**(2):326-337. http://dx.doi.org/10.1007/s10851-014-0525-0

Wu, H., Tian, G., Duan, P., *et al.*, 2013. The design of a novel artificial label for robot navigation. Proc. Chinese Intelligent Automation Conf., p.479-487. http://dx.doi.org/10.1007/978-3-642-38460-8_53

Xu, D., Tan, M., Li, Y., 2011. Visual Measurement and Control for Robots. National Defense Industry Press, Beijing, China, p.132-136 (in Chinese).

Yu, H.H., Hsieh, H.W., Tasi, Y.K., *et al.*, 2013. Visual localization for mobile robots based on composite map. *J. Robot. Mech.*, **25**(1):25-37.

Yuan, X., Song, M., Zhou, F., *et al.*, 2015. A novel Mittag-Leffler kernel based hybrid fault diagnosis method for wheeled robot driving system. *Comput. Intell. Neurosci.*, **2015**:606734.1-606734.11. http://dx.doi.org/10.1155/2015/606734

Zhang, Z., 2000. A flexible new technique for camera calibration. *IEEE Trans. Patt. Anal. Mach. Intell.*, **22**(11): 1330-1334. http://dx.doi.org/10.1109/34.888718